

# MORPHOLOGY AND DYNAMICS OF SOLAR PROMINENCES FROM 3D MHD SIMULATIONS

J. TERRADAS<sup>1</sup>, R. SOLER<sup>1</sup>, M., LUNA<sup>2,3</sup>, R. OLIVER<sup>1</sup>, J. L. BALLESTER<sup>1</sup>

<sup>1</sup>Departament de Física, Universitat de les Illes Balears, E-07122 Palma de Mallorca, Spain

<sup>2</sup>Instituto de Astrofísica de Canarias, E-38200 La Laguna, Tenerife, Spain and

<sup>3</sup>Departamento de Astrofísica, Universidad de La Laguna, E-38206 La Laguna, Tenerife, Spain

*Draft version December 24, 2014*

## ABSTRACT

In this paper we present a numerical study of the time evolution of solar prominences embedded in sheared magnetic arcades. The prominence is represented by a density enhancement in a background stratified atmosphere and is connected to the photosphere through the magnetic field. By solving the ideal magnetohydrodynamic (MHD) equations in three dimensions we study the dynamics for a range of parameters representative of real prominences. Depending on the parameters considered, we find prominences that are suspended above the photosphere, i.e., detached prominences, but also configurations resembling curtain or hedgerow prominences whose material continuously connects to the photosphere. The plasma- $\beta$  is an important parameter that determines the shape of the structure. In many cases magnetic Rayleigh-Taylor (MRT) instabilities and oscillatory phenomena develop. Fingers and plumes are generated, affecting the whole prominence body and producing vertical structures in an essentially horizontal magnetic field. However, magnetic shear is able to reduce or even to suppress this instability.

*Subject headings:* magnetohydrodynamics (MHD) — magnetic fields — Sun: corona

## 1. INTRODUCTION

Quiescent prominences are large structures of cool and dense plasma suspended in quiet regions of the solar corona. These structures can have lifetimes of weeks although they have a highly dynamic nature. It is generally believed that the mass in a quiescent prominence is supported against gravity by the magnetic Lorentz force. Different models of the magnetic structure of prominences have been proposed in the past (see the review of Mackay et al. 2010), and magnetic dips, i.e., sites where the magnetic field lines are locally horizontal and curved in the upward direction, are thought to play a relevant role. Examples of such configurations are the Kippenhahn & Schlüter (1957) model, hereafter referred as KS, or the Hood & Anzer (1990) model where dips are self consistently created by the weight of the heavy prominence. An alternative is that dips already exist before the dense material is deposited in them. In this context, there are models suggesting that prominences are supported by flux ropes that are essentially horizontal and lie above the polarity inversion line, (see Sakurai 1976; Low 1981; Rust & Kumar 1994, 1996; Low & Zhang 2004). Another possibility is that instead of a flux rope it is a sheared arcade that is responsible for the dips, c.f., Antiochos et al. (1994); Aulanier et al. (2002); DeVore et al. (2005); Karpen et al. (2005); Luna et al. (2012). However, the interplay between magnetic field and the dense prominence is not addressed in these works. In the present paper we investigate in a consistent way a magnetic shear arcade model together with a dense prominence, leaving the analysis of flux rope models for future studies.

The *Hinode* satellite has provided unprecedented high-resolution images of quiescent prominence allowing a de-

tailed study of the dynamics of these structures. Prominences show changes in morphology, irregular motions on different spatial and temporal scales, downflows, upflows, vortices, raising bubbles, plumes, etc. Berger et al. (2008, 2010) reported dark upflows that formed at the base of some quiescent prominences. Berger et al. (2010) proposed that these observed upflows were caused by the Rayleigh-Taylor instability (see Rayleigh 1883; Taylor 1950). Ryutova et al. (2010) showed how many fundamental plasma instabilities can be linked to dynamical processes occurring in prominences. In particular they showed that the development of regular series of plumes and spikes taking place at the interface between the prominence and corona are most likely related to the development of magnetic Rayleigh-Taylor (MRT) instabilities. Hillier et al. (2011) described how upflows can be the consequence of the MRT instability acting on the boundary between the KS prominence model and a tube inserted in the structure. Later, Hillier et al. (2012a) performed a detailed description of the dynamics of the system using the KS model for a wide range of model parameters. Hillier et al. (2012b) have extended the previous works to include interchange reconnection in the models. Dudík et al. (2012) have proposed that the existence of prominence bubbles is connected to a pair of magnetic null points associated with the prominence feet, and that a separator-reconnection scenario, which is very different from the Rayleigh-Taylor hypothesis, may naturally explain the bubble and plume formation. The role of neutrals on the MRT instability was investigated (in the linear regime) by Díaz et al. (2012) while Khomenko et al. (2014) have considered the non-linear regime and have found that the configuration is always unstable on small scales. The models presented by these authors are based on local models of prominences and the effect of the corona is not included. Moreover, the magnetic field does not connect to the photosphere

which is an important boundary condition for prominence support. In this paper these points are properly addressed.

Another example of dynamical phenomena reported in quiescent prominences are oscillations. These oscillations are either of global nature, producing motions of the whole prominence (see Tripathi et al. 2009; Li & Zhang 2012; Luna et al. 2014; Shen et al. 2014), or they are local. In this last case, the small amplitude periodic motions are mostly detected in Doppler shifts of spectral lines, see for example Tsubaki (1988); Oliver (1999); Oliver & Ballester (2002), and the reviews of Mackay et al. (2010) and Arregui et al. (2012). The theoretical understanding of the oscillations is based on the hypothesis that they correspond to magnetohydrodynamic (MHD) waves. An intense modeling of prominence oscillations has been done in the last years and it has been mostly based on the determination of the normal modes of different prominence models. These equilibrium models are rather simple and the configuration is represented by slabs or cylindrical tubes. It is important to remark that the MHD perturbations on these models are imposed to satisfy line-tying conditions at the photosphere. This is a crucial boundary condition that has a strong effect on the eigenmodes of the prominence and has important consequences regarding the stability of the structure. The importance of line-tying conditions on prominence oscillations is well known, and a self-consistent way of investigating the dynamics of prominences must involve the effect of the underlying photosphere (see Schutgens 1997; van den Oord et al. 1998).

In Terradas et al. (2013) a two-dimensional prominence model embedded in a coronal quadrupolar arcade was constructed to mimic a normal polarity prominence. In that work, dense material representing the prominence was injected in an initially stable magnetic structure increasing the gravitational energy. From the analysis of the evolution of the system it was found that in some cases the system relaxed towards a situation that was close to a stationary state. The obtained models using this method represent cool prominences supported against gravity by magnetic dips (see also the work of Hillier & van Ballegooijen 2013, who considered a two-dimensional flux rope model instead of an arcade configuration). The formation process (see the works of Xia et al. 2011, 2012; Keppens & Xia 2014) was not addressed in this model and the main aim was to study MHD waves on the generated models.

The main motivation in the present paper is to extend the study of the two-dimensional model of Terradas et al. (2013) to the three-dimensional case. Again our interest is on global models of prominences rather than in the details of the internal structure. Line-tying conditions are applied at the photosphere as they are crucial to have magnetic support and they strongly affect the dynamics of the system. Since the model is three-dimensional it allows us to analyze perturbations along the longitudinal axis of the prominence neglected in the 2D case. This changes significantly the physics of the system because MRT unstable modes are easily excited. The development of the instabilities together with the oscillatory behavior of the structure generate complex motions in the prominence body. One of the main aims of this work is to investigate the dynamics but also to understand how the

morphology of the prominence depends on the different parameters of the model.

## 2. INITIAL CONFIGURATION AND SETUP

The basic initial configuration is an isothermal stratified atmosphere as in Terradas et al. (2013). The same parameters have been used in the present work. The main difference is in the magnetic field configuration, which now has a component in the  $y$ -direction that introduces shear in the system. Again the force-free magnetic field is based on arcade solutions. The magnetic field has to satisfy

$$(\nabla^2 + \alpha^2) \mathbf{B} = 0, \quad (1)$$

where it has been assumed that  $\nabla \times \mathbf{B} = \alpha \mathbf{B}$  and  $\alpha$  uniform.

An arcade solution of Eq. (1) has the following magnetic field components

$$B_x(x, z) = B_0 \frac{l}{k} \cos kx e^{-l z}, \quad (2)$$

$$B_y(x, z) = B_0 \frac{\alpha}{k} \cos kx e^{-l z}, \quad (3)$$

$$B_z(x, z) = -B_0 \sin kx e^{-l z}. \quad (4)$$

where  $B_0$  is a reference constant. The parameter  $k$  is related to the lateral extension of the arcade while  $l$  is a measure of the vertical magnetic scale height. The parameter  $\alpha$  is given by the following expression

$$\alpha = (k^2 - l^2)^{1/2}, \quad (5)$$

and it is related to the amount of shear in the arcade. For  $l = k$ ,  $\alpha = 0$ , the magnetic field is purely potential and the  $B_y$  component is zero.

Magnetic field lines in the configuration given by Eqs. (2)-(4) do not show any dips because the configuration is bipolar. A simple way to obtain a configuration with magnetic dips it to chose a particular superposition of two magnetic arcades representing a quadrupolar configuration

$$B_x(x, z) = B_1 \frac{l_1}{k_1} \cos k_1 x e^{-l_1 z} - B_2 \frac{l_2}{k_2} \cos k_2 x e^{-l_2 z}, \quad (6)$$

$$B_y(x, z) = B_1 \frac{\alpha}{k_1} \cos k_1 x e^{-l_1 z} - B_2 \frac{\alpha}{k_2} \cos k_2 x e^{-l_2 z}, \quad (7)$$

$$B_z(x, z) = -B_1 \sin k_1 x e^{-l_1 z} + B_2 \sin k_2 x e^{-l_2 z}. \quad (8)$$

The individual arcades, quoted with the sub-indexes 1 and 2, must have the same  $\alpha$  to satisfy the Helmholtz equation given by Eq. (1). Thus, we have according to Eq. (5) the constraint

$$k_1^2 - l_1^2 = k_2^2 - l_2^2. \quad (9)$$

The width of the full structure is  $L_a$ , and we select the following wavenumbers  $k_1 = \pi/2L_a$  and  $k_2 = 3\pi/2L_a$  since they generate a magnetic configuration with dips at  $x = 0$ . The parameter  $l_1/k_1$ , hereafter referred as  $l/k$ , is related to the amount of shear in the structure. Several examples of different sheared arcades are found in Fig. 12 by imposing the previous wavenumbers and that  $B_2 = B_1$ . Note the location of dips and that the magnetic configuration is invariant in the  $y$ -direction.

The initial prominence mass and size are prescribed according to typical values reported from observations (see for example Labrosse et al. 2010). Here we assume that the typical size of the density enhancement has a width of  $5 \times 10^3$  km, a length of  $4 \times 10^4$  km, and a height of  $10^4$  km. The prominence is initially suspended above the photosphere at a height of  $1.75 \times 10^4$  km. With a typical prominence density of  $5.2 \times 10^{-2} \text{ kg km}^{-3}$  and taking into account the geometry of the prescribed prominence (see Fig. 1 top panel), the total mass is  $1.3 \times 10^{11}$  kg. For this case the density contrast between the corona and the core of the prominence is around 120. In some simulations we have changed the total mass of the prominence by reducing the density contrast. Between the core of the prominence and the corona we have included in the initial density profile a prominence-corona transition region (PCTR) with a typical width of 30 – 15% of the characteristic length in each direction. The mass deposition is produced just at  $t = 0$  and contrary to the situation in Terradas et al. (2013) the deposition is instantaneous.

Note that there is no initial velocity perturbation introduced in the system. However, because of the mass deposition at  $t = 0$  the system immediately reacts to the presence of the enhanced mass which is pushed down by the gravity force, and therefore velocity perturbations, specially in the vertical component, will be generated.

### 3. NUMERICAL TOOLS

The code used to solve the ideal MHD equations is an evolution of the code MoLMHD already described in Terradas et al. (2013) (see also Bona et al. 2009). The main novelty in the present version is the implementation of a WENO scheme (see for example the review of Shu 2009) to solve some of the MHD equations (see Jiang & Wu 1999; Balsara et al. 2009). In particular we have used a fifth order accurate method in space to solve the equations of continuity, momentum and energy. This last equation has been written in terms of gas pressure instead of total energy. The WENO scheme is very robust with respect to the presence of stiff gradients in the variables and thus suitable to handle strong shocks. The density contrast between the prominence and corona can be higher than 100, and therefore difficult to treat without high-resolution numerical methods. Nevertheless, for the induction equation we have used a standard fourth order central discretization with an artificial dissipation coefficient since the application of the WENO scheme on the magnetic field has been found to be too diffusive. The excess of diffusion produces plasma motions across the magnetic field changing the dynamics with respect to the idealized case where plasma is frozen to the magnetic field. The inevitable numerical diffusion associated to the scheme has been significantly reduced with the method used in this paper.

The MHD equations solved in this study are

$$\begin{aligned} \frac{\partial \rho}{\partial t} + \nabla \cdot (\rho \mathbf{v}) &= 0, \\ \frac{\partial \rho \mathbf{v}}{\partial t} + \nabla \cdot \left( \rho \mathbf{v} \mathbf{v} + p \mathbf{I} - \frac{\mathbf{B} \mathbf{B}}{\mu} + \frac{\mathbf{B}^2}{2\mu} \right) &= \rho \mathbf{g}, \\ \frac{\partial \mathbf{B}}{\partial t} &= \nabla \times (\mathbf{v} \times \mathbf{B}), \end{aligned}$$

$$\frac{\partial p}{\partial t} + \nabla \cdot (\gamma p \mathbf{v}) = (\gamma - 1) \mathbf{v} \cdot \nabla p,$$

where  $\mathbf{I}$  is the unit tensor,  $\mathbf{g}$  is the gravitational acceleration, and the rest of the symbols have their usual meaning.

As in Terradas et al. (2013) the technique of background splitting for the magnetic field (see Powell et al. 1999) has been used and this has allowed us to gain numerical accuracy. The splitting introduces source terms in the equations that have been treated using the fourth order central scheme. Although in Powell et al. (1999) it is assumed that the initial magnetic field is potential, i.e., current free, it turns out that for a magnetic field that is not potential the corresponding source terms are exactly the same.

Regarding boundary conditions we have applied line-tying at the bottom plane, representing the photosphere. This condition means that the three components of the velocities are set to zero while the normal component of the magnetic field,  $B_z$  in our Cartesian system, is fixed. For the rest of the variables at this boundary we have used simple extrapolation, i.e., that their spatial derivatives are zero. For top and lateral boundaries we expect the energy to escape the system. We have tested different conditions. Using decomposition in characteristics fields at the boundary (see Terradas et al. 2013) works fine but it is computationally expensive. We have found that using fixed values at the boundary essentially produce the same results as the decomposition in characteristics, and it is much more simple to implement. This last approach has already been used in Török & Kliem (2003); Török et al. (2004) in the context of ideal kink instabilities in magnetic loops.

The reference length in the simulations is  $L = 10^4$  km and the width of the arcade is  $L_a = 6L$ . Velocities have been normalized to the coronal sound speed at a temperature of 1 MK,  $c_{s0} = 166 \text{ km s}^{-1}$ . The reference time is  $\tau = L/c_{s0} = 1 \text{ min}$ . The total time of evolution is 100 min. The typical resolution that we have used in the simulations is  $150 \times 150 \times 100$  points, with  $-6 < x/L < 6$ ,  $-6 < y/L < 6$ , and  $0 < z/L < 8$ , being  $L = 10^4$  km the reference length. Higher resolutions have been also considered to see the effect on the results. Since we consider a global prominence model we need, from the numerical point of view, to have enough grid points in both the coronal part and the prominence body. The typical distance between grid points is 800 km but in some cases it has been reduced to 550 km. Structures of the size of individual threads are not resolved in this work.

## 4. RESULTS

### 4.1. A typical run

The results of a typical simulation are displayed in Fig. 1. In this figure the density distribution and some specific magnetic field lines are plotted as a function of time (see also Movie1 in the electronic version of the paper). During the first hour of evolution the prominence body is able to be suspended above the photosphere due to the force provided by the magnetic field. The structure resembles a detached prominence, referred in the past as a suspended cloud. Although there is global support, the shape of the prominence changes with time. We

can see that for example after 30 min of evolution, small scales appear in the density distribution which was initially quite homogeneous. This is linked to the excitation of MRT instabilities. Changes in density involve variations of the magnetic field since the plasma is frozen to the magnetic field in ideal MHD. Therefore the motion of magnetic field lines has to be consistent with plasma motions (see Movie2).

At a given instant, temperature and plasma- $\beta$  distributions ( $\beta$  is the coefficient between gas and magnetic pressure) are quite irregular due to the presence of the cool and dense material representing the prominence. The distribution of these magnitudes at the central plane is plotted in Fig. 2. We find that density variations produced during the evolution also involve temperature changes. Temperature is typically of the order of 10 000 K inside the prominence while in the corona is around 1 MK. Between these two regions we find the PCTR, clearly visible in temperature. In this configuration the plasma- $\beta$  changes mostly with height, it has a minimum around the prominence location and increases toward the photosphere and upwards with height. At the the prominence core it is below 0.02.

The dynamics of the system is quite rich and several features need to be described in detail. For example, the prominence shows oscillations before the clear onset of the MRT instability. In Fig. 3 the vertical component of the velocity at early stages of the simulation is represented at the plane passing through the prominence core. At the center of the prominence the velocity at  $t = 2.88$  min is negative since the prominence body is moving downwards. In the following frame, at  $t = 5.76$  min the motion is in the positive vertical direction. This is a consequence of the vertical oscillatory motion that the whole prominence is doing during the relaxation process. Note also the deformation of the lower boundary of the prominence displaying a convex curve for  $t = 8.64$  min. At the same time strong shear motions are generated at the lateral edges of the prominence where we find positive/negative velocity patterns in  $v_z$ . The spatial scales of these patterns decrease with time as can be appreciated in Fig. 3. This has to do with the process of mode conversion and phase-mixing that takes place at the inhomogeneous layers of the structure, in this case the prominence PCTR at the sides of the prominence body in the  $y$ -direction. Part of the attenuation of the oscillatory vertical motion of the structure is due to this process, however, wave leakage might play a role as well. Since our aim is to concentrate on the global evolution of the system we leave the analysis of oscillations and damping for future studies. However, it is interesting to mention that these shear motions at the edges of the prominences may lead to the development of another type of instabilities due to velocity shear, i.e., Kelvin-Helmholtz instabilities. Indeed, a closer inspection of the lateral edges of the prominence indicate the presence of very dynamic motions at the PCTR associated to this kind of instability, but with the particularity that shear changes periodically with time due to the global oscillation of the structure. This effect is similar to the deformations produced at the boundaries of a cylindrical tube when it is oscillating (see Terradas et al. 2008).

At the beginning of the simulation there are no clear

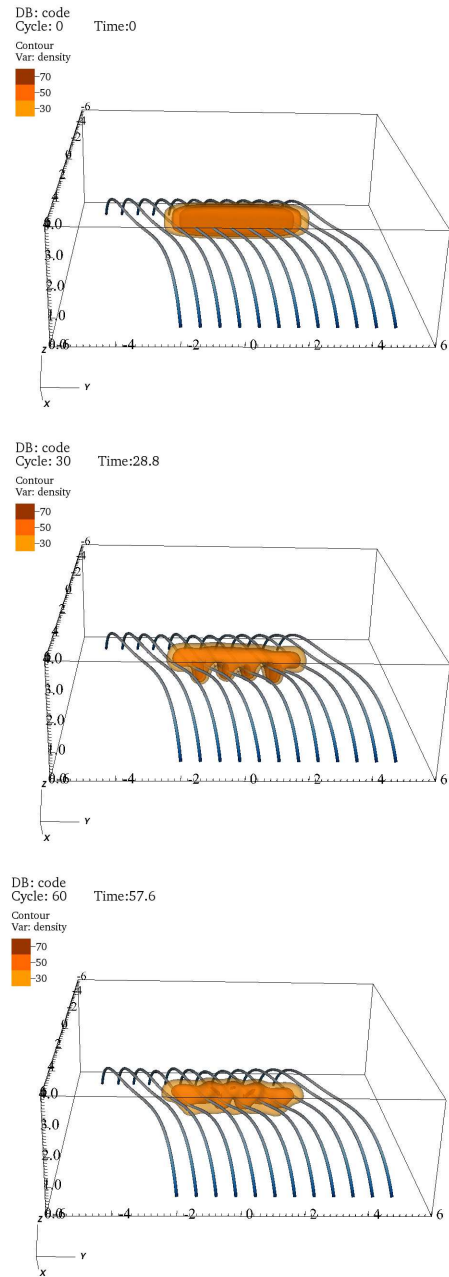


FIG. 1.— Time evolution of density and magnetic field lines for a typical case. In this simulation  $l/k = 0.95$  (weak shear), and  $v_{A0} = 20 c_{s0}$ , being  $v_{A0} = B/\sqrt{\mu\rho_0}$  the maximum Alfvén speed in the system. The maximum magnetic field ( $B$ ) corresponds to the points  $x = \pm L_a$  and  $z = 0$ . Density is normalized to the coronal density ( $\rho_0$ ). Time in minutes is shown at the top of each panel. See also Movie1 in the online material.

signatures of MRT unstable modes. Instabilities start to develop around  $t = 20$  min, as can be appreciated in Fig. 4. Apart from the shear motions associated to the lateral edges of the prominence and explained before, we also find shear motions in the vertical component of the velocity that start to form at the bottom part of the prominence (see positive/negative velocity patterns). These vertically shear motions now produce strong deformations of the bottom of the prominence, clearly visible in density in Fig. 4. Descending fingers of

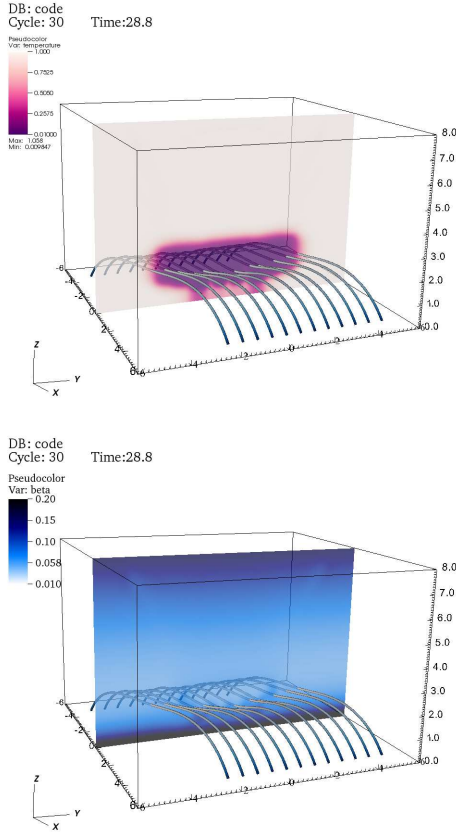


FIG. 2.— Temperature and plasma- $\beta$  at the plane passing through  $x = 0$  for the simulation shown in Fig. 1 at  $t = 28.8$  min. Temperature is normalized to the coronal value, 1 MK.

cool and dense plasma and ascending plumes of hot and less dense plasma have been developed in the structure and modify significantly the density distribution of the prominence. For the particular simulation studied here the prominence bottom shows several arches that spread all over the prominence body. In particular we can identify up to four clear fingers. The density and  $v_z$  distribution is further visualized in Fig. 5 (see also Movie2). The excitation of MRT unstable modes affects the prominence on a global scale and the instability is modified by the effect of line-tying conditions. For the simulation shown in Figs. 4 and 5 the growth time of the instability is of the order of 20 min. This estimation is based on the change in position of the finger-like structures in the prominence but it is important to remark that during the evolution of the MRT instability the prominence is still oscillating (see Movie2) and this complicates the estimation of growth-rates. Thus, this growth time does not correspond to the growth time that one would calculate in the linear stage of development of the instability. Nevertheless, it is a useful parameter since it gives a typical time scale associated to the physical process. It is worth to mention that in this simulation the prominence is not destroyed by the instability at least during the first 100 min of evolution. The eventual destruction of the prominence in a short period of time would mean that indeed a continuous supply of material is required as some observations suggest.

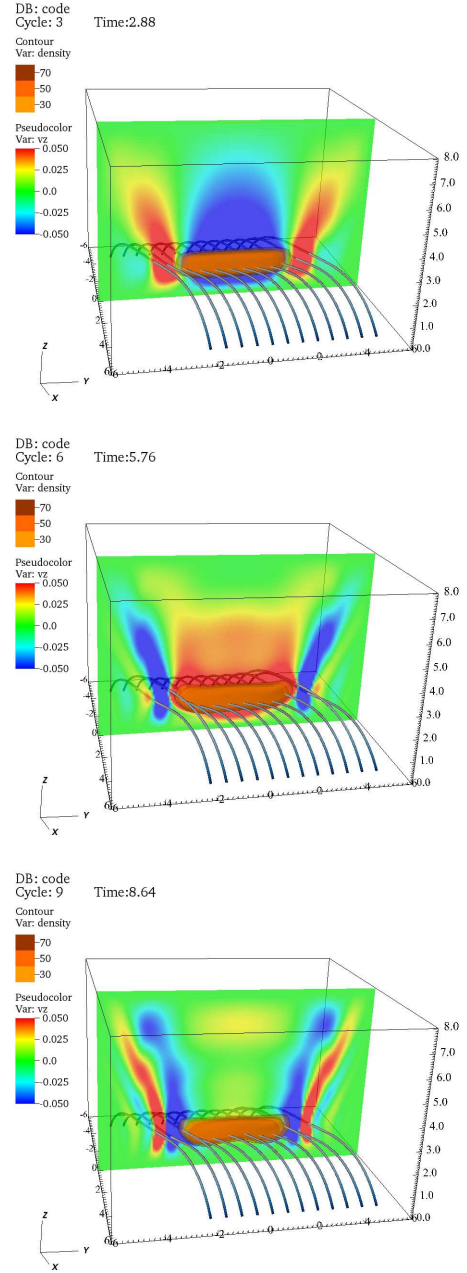


FIG. 3.— Time evolution of density and vertical velocity at the  $yz$ -plane at  $x = 0$  during the first 12 min of evolution before the onset of the instability. Shear vertical motions are produced at the boundaries of the prominence during the oscillations. Velocity amplitudes are normalized to the coronal sound speed.

Further information about the dynamics of the system is derived from the behavior of the energy. We have calculated from the simulations the integrated kinetic energy at the plane  $yz$ -plane ( $x = 0$ ). This magnitude is useful since it shows clear signatures of the development of instabilities associated to MRT unstable modes. In Fig. 6 the total kinetic energy (continuous line) and the energy associated to the vertical velocity component (dotted line) are plotted as a function of time. According to the plot, most of the kinetic energy is due to vertical motions which are initially induced by the gravity force.



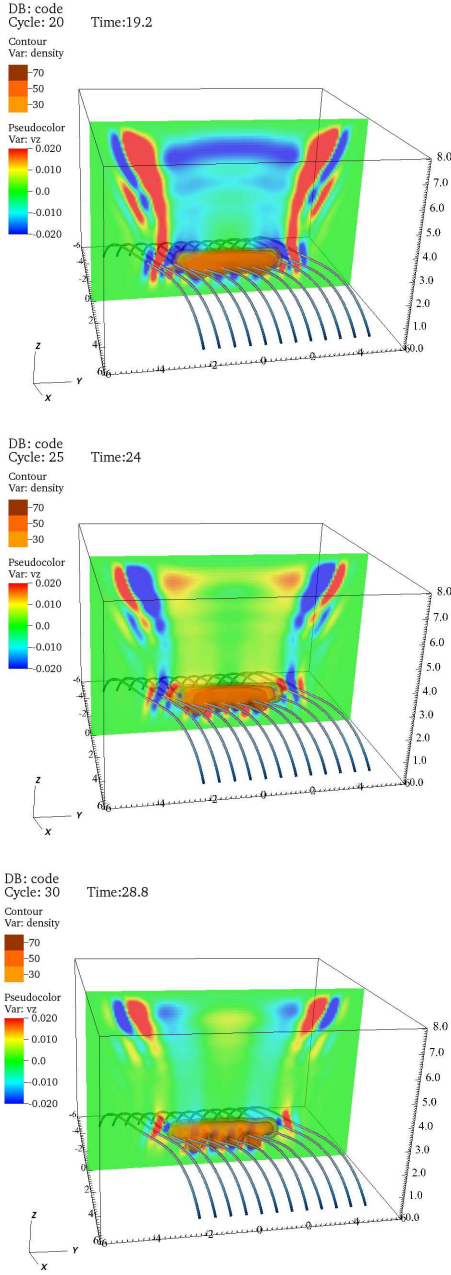


FIG. 4.— Time evolution of density and vertical velocity at the  $yz$ -plane at  $x = 0$  during the development of the MRT instability.

The energy decreases with time due to the effect of leakage while the prominence is oscillating vertically (see the fluctuations in the dotted line for  $t < 20$  min). Later, around  $t = 25$  min the kinetic energy starts growing, this is the indication of the development of the instability and coincides with the appearance of the fingers and plumes in density (see for example, Fig. 1 middle panel, or Movie1). After peaking around  $t = 32$  min the energy starts decreasing again, meaning that fingers do not continue moving toward the photosphere at the same velocity, in fact they are decelerating. In the energy profile (and this can be also identified in Movie1) there is a faint indication about a new development of the instability around  $t = 60$  min. Therefore in this par-

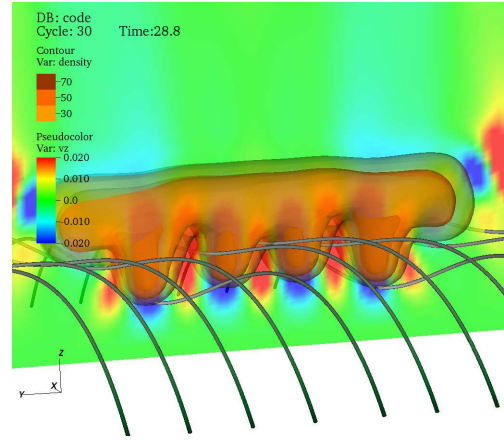


FIG. 5.— Zoom of density and vertical velocity at a given time (see Fig. 4 bottom panel). Fingers and plumes associated to the MRT instability are present and are associated to the shear motions in velocity. Some magnetic field lines are also represented. See Movie2 in the online material.

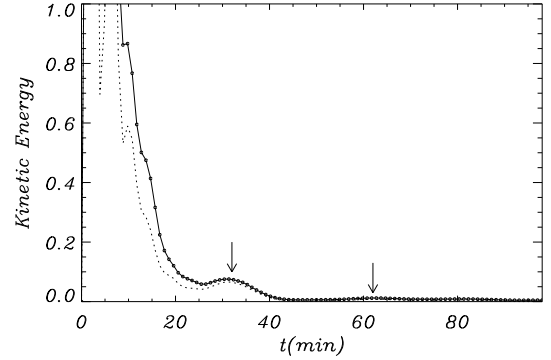


FIG. 6.— Integrated kinetic energy at the  $yz$ -plane at  $x = 0$  as a function of time. The continuous line represents the total kinetic energy while the dotted line corresponds to the kinetic energy in the vertical direction only. The arrows show times when the MRT instability is clearly identified.

ticular example the instability is unable to destroy the prominence although it produces dynamic motions at the prominence body.

The MRT unstable interface between the prominence and corona has smooth density gradients due to the presence of the PCrTR. It is well known that density gradients have the effect of reducing the growth rate of RT instabilities, especially at short wavelengths (see for example Mikaelian 1986). We have performed a run with half the size of the PCrTR in the standard simulation but the differences in the spatial scales of the instability and the growth rates are not too significant. Although we start with a given width of the PCrTR, after the time-evolution the eventual “quasi-equilibrium” that is obtained has a thicker transition between the core of the prominence and corona since radiation and conduction are neglected in the model. The magnetic field also has gradients and Yang et al. (2011) have shown that they affect the linear growth rates of the MRT instability in a certain range that depends on the magnetic field strength. Thus, the excitation of the most unstable mode with a particular spatial scale, in our case we find structures with typically

three cavities, will be conditioned by all these effects and it is very difficult to anticipate. However, we think that the most important factors that affect the appearance of the unstable modes and the spatial distribution of the cavities in the horizontal direction are the strength of the magnetic field at the core of the prominence and the variation of the shear angle with height. This will be studied in Section 4.4. It is worth to mention that due to the symmetry of the system there is a maximum in velocity at the center of the prominence (in the  $xz$ -plane at  $y = 0$ ). This means that there is a natural excitation of symmetric modes in velocity respect to the center of the prominence. For this reason it is logical to find structures with an odd number of cavities along the  $y$ -direction (three in the case of Fig. 1).

The spatial patterns related to the MRT instability found in the simulations may have a close link with the observed arches and cavities reported in many prominences, see for example Berger et al. (2010). It is worth to mention that in Berger et al. (2010) the cavities beneath the prominence are found forming single structures instead of multiple cavities like in the present simulations. However, the vertical structuring observed in many polar crown prominences (see for example Dudík et al. 2012) resembles the spatial structures found in the simulations. Ryutova et al. (2010) associated the appearance of bubbles/cavities to the development of screw-pinch instabilities assuming helical prominence models. However, if the structure does not have a clear flux rope shape and it is better represented by a sheared arcade, then the MRT instabilities found in our simulations can provide an explanation for the formation of cavities. In this regard, MRT instabilities have been already investigated using 3D simulations by Hillier et al. (2011, 2012a,b). Since these authors have focused on internal motions the connection of the field lines with the photosphere was neglected in their models, and as we have already anticipated line-tying conditions change considerably the dynamics of the MRT instability. The MRT instability in our configuration affects the whole prominence body, instead of small internal parts. However, it must be pointed out that due to the limitation in the numerical resolution, we are unable to resolve features with the spatial scales studied by Hillier et al. (2011).

#### 4.1.1. Effect of boundary conditions

For the simulations presented here line-tying conditions have been imposed at the photosphere. Without this condition at  $z = 0$ , the core of the prominence would simply fall due to the effect of gravity, and the associated changes of the local magnetic field would be unable to provide magnetic support. We have performed several simulations to check this effect by removing line-tying photospheric conditions and indeed we have not been able to find a sustained prominence. Thus, the effect of the communication between the prominence and the photosphere due to the reflecting conditions cannot be neglected since it is very relevant regarding the support of the prominence against gravity. This is an important property of the simulations performed in this work. We plan to study in the future other boundary conditions such as mirror boundaries or boundaries using potential field extrapolations. In fact, the photospheric magnetic

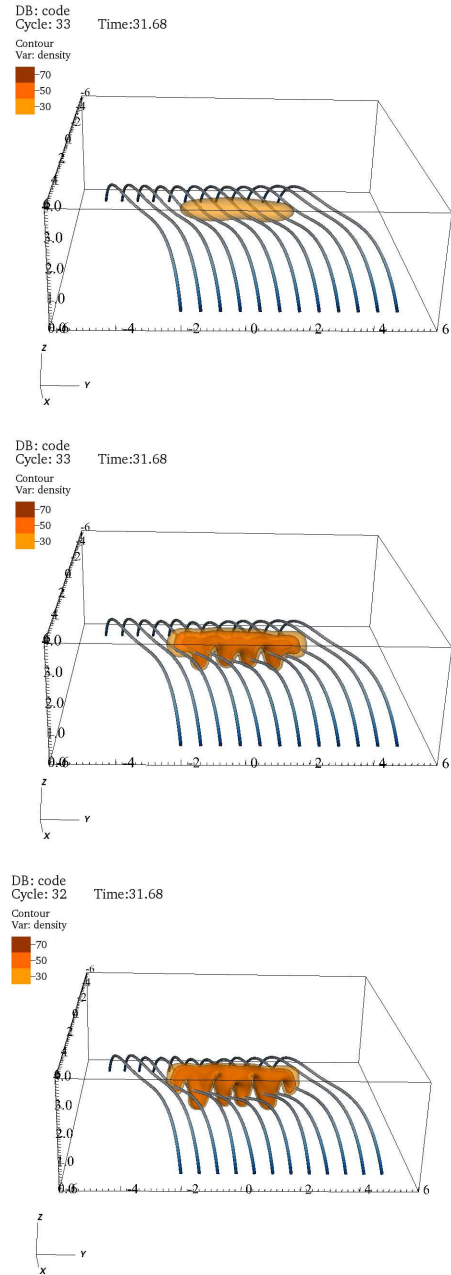


FIG. 7.— Prominence density and magnetic field for three different values of the numerical resolution,  $75 \times 75 \times 50$ ,  $150 \times 150 \times 100$ , and  $225 \times 225 \times 150$ . Time is essentially the same for the three simulations. All the other parameters are the same as in Fig. 1.

field may change over timescales of a few hours due to photospheric convective motions. Nevertheless, we have decided to concentrate on the most simple boundary conditions that lead to sustained prominences, i.e., line-tying conditions.

We have also checked the effect of the location of the lateral and upper boundaries. We have concluded that locating these boundaries at larger distances from the prominence body does not change significantly the results. For this reason, we have kept the boundaries located at the distances given in Sect. 3 in order to avoid a significant decrease in the numerical resolution when a

fixed number of grid points is used.

#### 4.1.2. Effect of numerical resolution

The complex dynamics of the instability depends on the resolution of the numerical simulation. To show this effect we have plotted in Fig. 7 the results at the same instant for three different numbers of grid points. With a low number of points, although there is still magnetic support, the instability is simply unresolved and density is too smoothed by the 5th order WENO scheme (see that high density isocontours are missing). When the resolution is improved spikes and plumes appear and the instability is resolved. Note also that with the highest resolution the instability has developed at a faster rate than at the intermediate resolution. This is due to decrease of the numerical dissipation when resolution is increased. Along the same lines, it must be pointed out that the instability will produce a cascade of energy to smaller spatial scales. If the small scales are not properly resolved this cascade of energy will not proceed at the appropriate rate and at some point a saturation will be achieved being the numerical dissipation dominant. This has prevented us from performing long runs in which the solution is too degraded, and have only focused on the evolution for about 100 min. Future studies should include nonuniform grids or adaptive mesh refinement (AMR) to resolve spatial scales smaller than 550 km, and to have a better estimation of the growth rates.

#### 4.2. Dependence on $\beta$

The case analyzed in Sect. 4.1 corresponds to a particular set of parameters. It is interesting to study how the evolution of the system depends, for example, on the strength of the magnetic field. In Fig. 8 the morphology of the prominence at a fixed time is shown for three different values of the plasma- $\beta$  associated to different magnetic field strengths at the core of the prominence. In the top panel we find the previous situation where the magnetic field is able to provide the support to the dense material against gravity. This case corresponds to a value of  $\beta = 0.075$  at the end of the simulation. This prominence can be classified as detached. Middle and bottom panels show a rather different scenario, and they are associated to  $\beta = 0.15$  and  $\beta = 0.4$ , respectively. In these last two cases the magnetic field is unable to provide the restoring force to hold the whole prominence suspended above the photosphere. Most of the dense plasma falls down and essentially pushes down the magnetic field near the photosphere (see the field lines crossing the center of the prominence body in Fig. 8). For  $\beta = 0.15$  some voids in density are appreciated at the center resembling some hedgerow prominences reported in observations (see the classification of prominences by Menzel & Evans 1953; Jones 1958; Zirin 1998). For the case  $\beta = 0.4$  the structure seems more compact resembling mound or curtain prominences with little structure. Note that if the view of the prominence is along the  $y$ -direction then it can resemble a pillar prominence which is simply a curtain prominence seen edge-on.

Details of the evolution for the curtain-like prominence are found in Figs. 9 and 10 (see also Movie3). In these figures we have represented the evolution of density and the  $x$ -component of the velocity,  $v_x$ , passing through

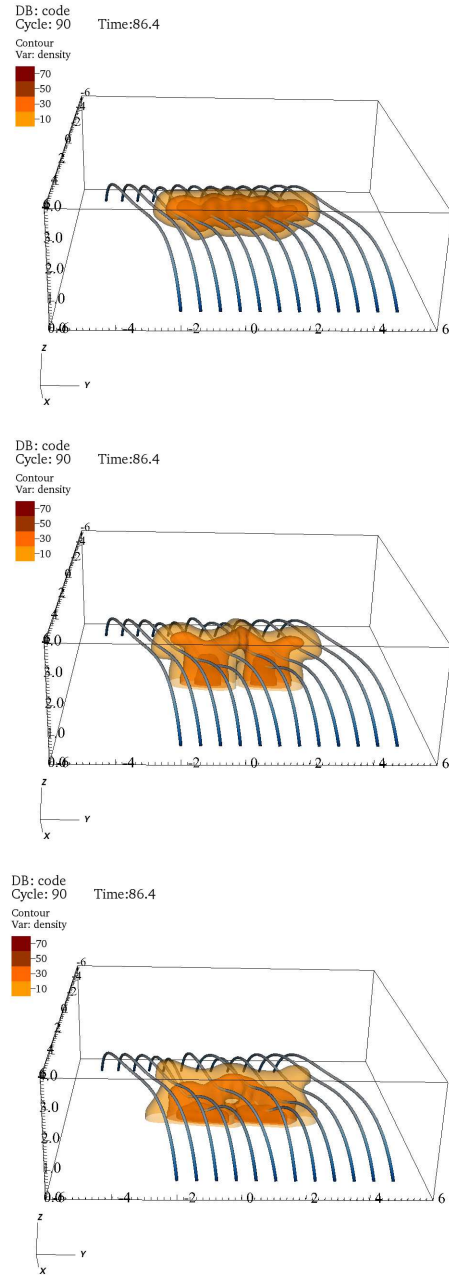


FIG. 8.— Prominence density and magnetic field for three different values of the magnetic field ( $v_{A0} = 20 c_{s0}$ ,  $v_{A0} = 15 c_{s0}$ , and  $v_{A0} = 10 c_{s0}$ ) which are associated to the values of  $\beta$  of 0.075, 0.15, and 0.4 at the core of the prominence. Time is the same for the three simulations.

the central plane. The other velocity components are also important at the beginning of the simulation but at the end of the simulation  $v_x$  dominates. At early stages of the evolution the behavior is quite involved, as can be appreciated at the top panel of Fig. 10, velocities up to  $4 \text{ km s}^{-1}$  are found at the edges but also at the core of the prominence. Outside the prominence we identify the emission of MHD waves, this is specially clear near the top of the domain where several wavefronts are visible. As time progresses the amplitudes of the motions decrease both at the prominence and in the corona. This decrease in the velocity amplitudes is mostly due to the



energy leakage that takes place at the upper and lateral boundaries of the computational domain. Numerical dissipation, although small, also contributes to the attenuation of the motions. At later stages of the evolution, see for example bottom panel of Fig. 10, we can still find some velocity signals at the prominence which are related, in this particular example, to a slow change in orientation of the axis of the prominence since the motions in the  $x$ -direction alternate sign with respect to the center of the structure.

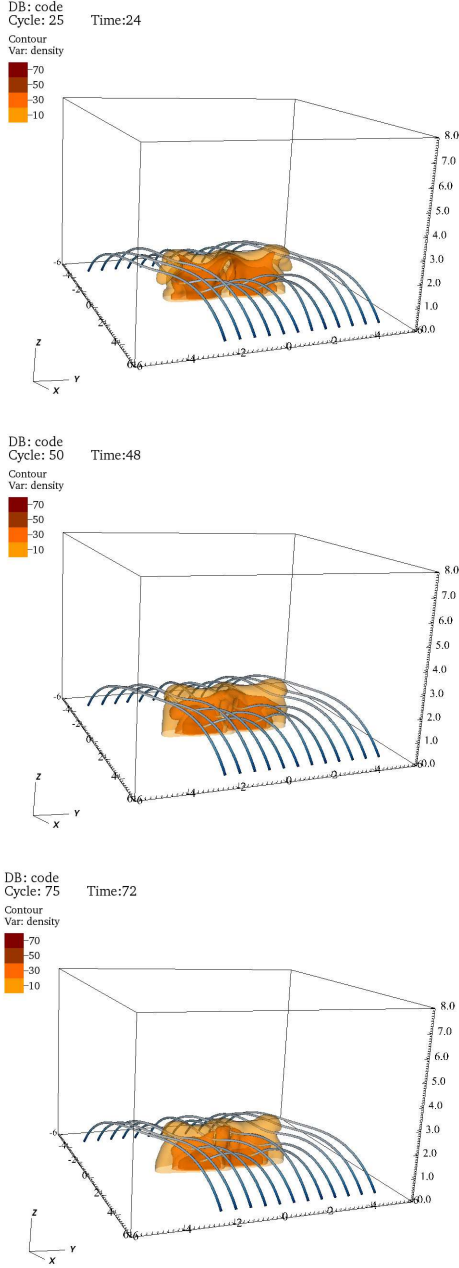


FIG. 9.— Details of the evolution of the prominence density for the case  $v_{A0} = 10c_{s0}$ . See also Movie3 in the online material.

#### 4.3. Dependence on prominence mass

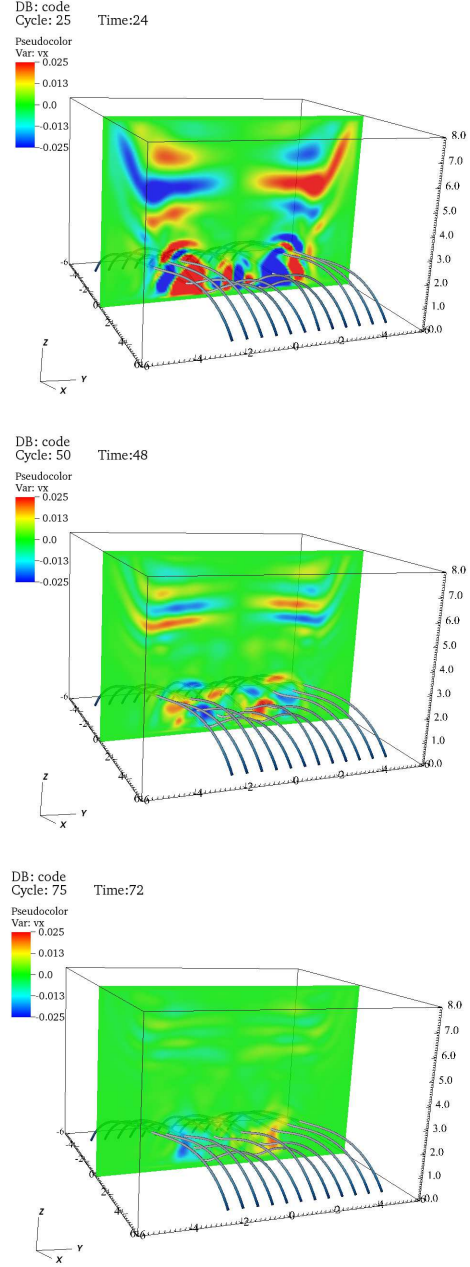


FIG. 10.— Details of the evolution of the horizontal component of the velocity ( $v_x$ ) for the case  $v_{A0} = 10c_{s0}$  and the same simulation as in Fig. 9.

Another relevant parameter is the total mass of the prominence. We have imposed a fixed strength of the magnetic field at the base of the arcade,  $v_{A0} = 10c_{s0}$ , and have decreased the prominence mass with respect to the mound prominence studied in Figs. 9 and 10. Now the total mass is four times lower, i.e., of the order of  $3.25 \times 10^{10}$  kg which is still in the range of masses calculated from observations (typically between  $10^9 - 10^{12}$  kg). Three snapshots of the density and magnetic field are plotted in Fig. 11 for this case. Although the plasma- $\beta$  at the core of the prominence is around 0.3, the magnetic structure is able to sustain the prominence suspended above  $z = 0$ , obtaining a detached structure. Thus, the total mass loading of the prominence essentially deter-

mines, together with the plasma- $\beta$ , the morphology of the structure. Note also the appearance of the MRT instability with some fingerprints visible in Fig. 11.

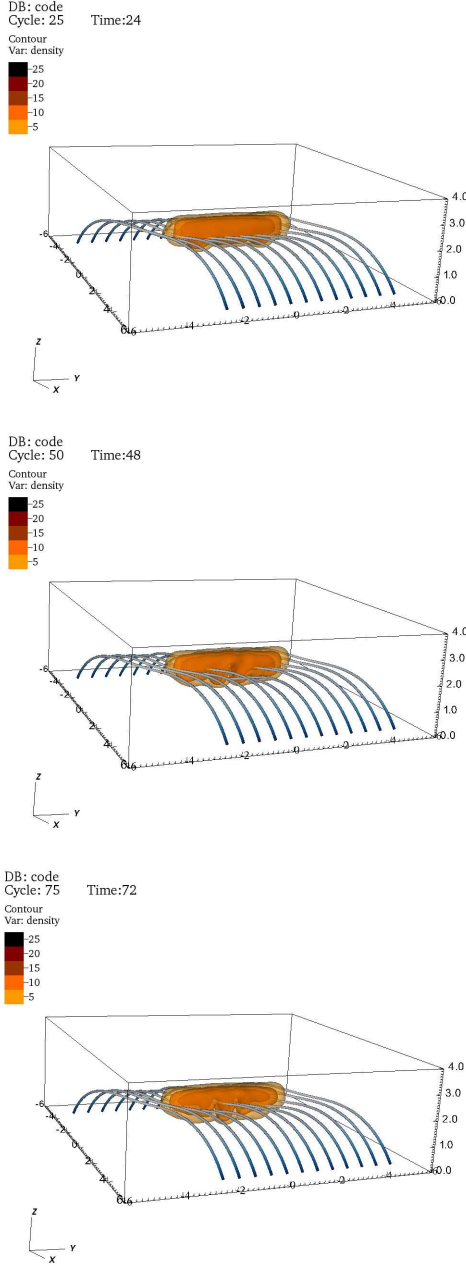


FIG. 11.— Details of the evolution of the prominence density for the case  $v_{A0} = 10 c_{s0}$  but for a total prominence mass that is four times smaller than in the previous cases. The density contrast between the prominence and corona is only 30 in this simulation.

#### 4.4. Dependence on magnetic shear

A parameter that can be also changed in the configuration is the amount of shear in the arcade. We have performed a set of different simulations by changing this parameter and the results are found in Fig. 12. For example, the MRT instability already developed for the case

$l/k = 0.95$  at  $t = 29.1$  min (see Fig. 1 middle panel) is not present for the arcade with  $l/k = 0.85$ . For larger values of the shear the global shape of the prominence does not change much from the side view of Fig. 12. This means that shear helps to have a more stable configuration regarding the MRT instability. In order to quantify this effect we have plotted in Fig. 13 the estimated growth-rates for different values of  $l/k$ . The unsheared arcade, the case  $l/k = 1$ , has the shortest growth-time which is around 20 min. The curve shown in Fig. 13 indicates that the growth-time increases with shear, meaning that this parameter helps to reduce the instability. Note that the dependence of the growth-times with shear can be quite strong, and that a small amount of shear may significantly reduce the instability. For example, we see that for values of  $l/k$  below 0.92 the growth-times are larger than 2 hours. For this equilibrium parameter the arcade is still weakly sheared since it would be an intermediate case between the cases  $l/k = 0.95$ , see Fig. 1, and  $l/k = 0.85$ , represented in Fig. 12 top panel.

We have investigated the reasons of the stabilization effect produced by an increase in magnetic shear. We have found basically two reasons. The first one is related to the strength of the magnetic field at the prominence body. It turns out that a decrease in the parameter  $l/k$  (increase in shear) produces an increase in the horizontal component of the magnetic field at the prominence. For example, for  $l/k = 0.65$  the horizontal component is 1.4 times larger than for  $l/k = 0.95$ . Stronger horizontal magnetic fields at the core of the prominence lead to a larger magnetic tension, and this is the force that helps to stabilize the MRT unstable modes. The second reason is related to the change of the shear angle with height. The effect of shear on MRT instabilities has been recently investigated analytically by Ruderman et al. (2014) in a much more simple geometry, a 2D slab configuration (in the  $xz$ -plane) with a discontinuous change in the magnetic shear and including propagation in the perpendicular direction (the  $y$ -direction). These authors have found that the growth rate is bounded under the presence of magnetic shear. The important result is that for small shear angles the growth time of the most unstable mode is linearly proportional to the shear angle, while in the limit of large angles the growth time is essentially independent of the shear angle. In our arcade configurations the situation is more complex since the magnetic shear changes smoothly with height (see Fig. 14). This must affect the growth times of the instability. Using the results of the simple slab model we can explain the qualitative behavior in the growth times with the parameter  $l/k$ . For  $l/k$  large, the variation of shear with height is relatively small (see in Fig. 14 the region around the prominence location, i.e., around  $z = 2$ ), meaning that the effective shear is small. Under such conditions the growth time is small (fast development of the instability). On the contrary, when  $l/k$  is small the change of shear with height is stronger (see Fig. 14) meaning that the effective shear is larger and thus the growth time is longer. This provides a qualitative agreement with the results shown in Fig. 13.

In fact, an increase in shear changes the depth of the dips, i.e., the vertical distance between the dip centre and the highest point on a magnetic field line, and it also changes the width of the dips. In Fig. 15 the magnetic

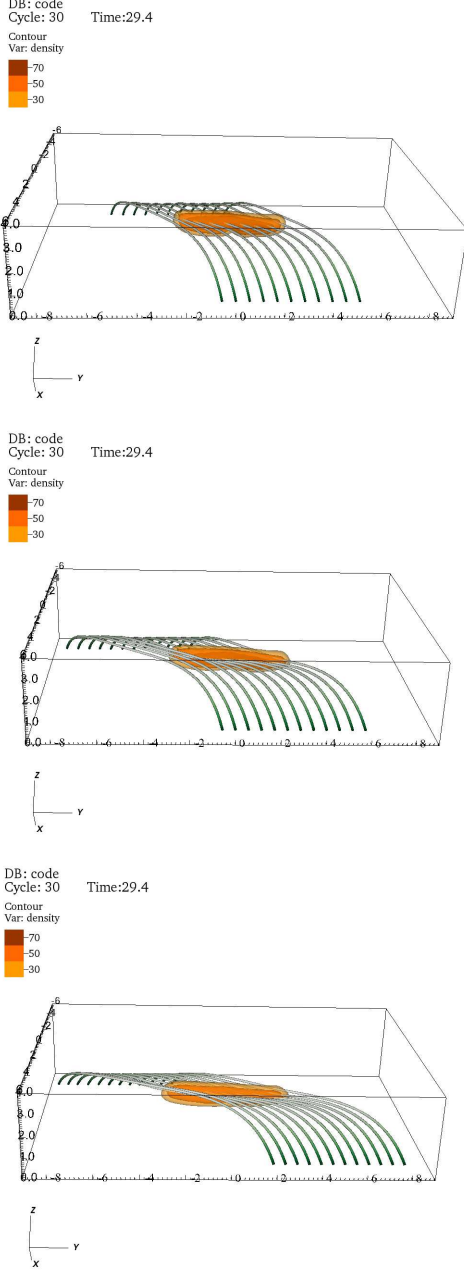


FIG. 12.— Density and magnetic field distribution for three different values of the magnetic shear,  $l/k = 0.85$ ,  $l/k = 0.75$ ,  $l/k = 0.65$ , that correspond to typical shear angles of  $32^\circ$ ,  $41^\circ$ , and  $54^\circ$ , respectively. The width of the domain in the  $y$ -direction is larger than in the previous simulations since an increased shear leads to longer field lines.

field lines (projected in the  $xz$ -plane) crossing the initial density distribution at a given height are plotted for two different values of the shear. For the case  $l/k = 0.95$  (continuous lines) we see that the field lines are quite flat at the top of the prominence and the depth of the dip increases as we move toward the photosphere. For the configuration with  $l/k = 0.65$  (dashed lines) with a much stronger shear the situation is different, at the top of the prominence the field lines are more curved than for  $l/k = 95$  and potentially less favorable to support the dense material, but as we move to lower heights the

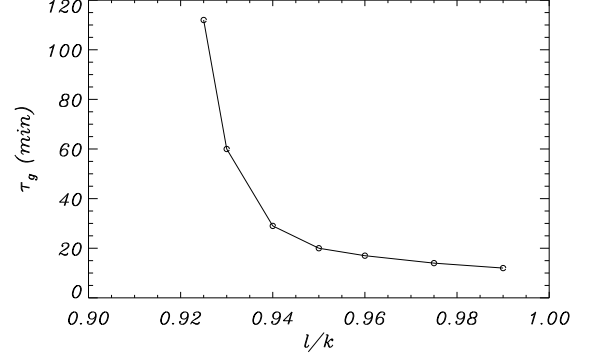


FIG. 13.— Growth-time of the dominant unstable MRT mode as a function of  $l/k$ . The case  $l/k = 1$  corresponds to the situation without shear. For  $l/k < 0.9$  the magnetic structure is unable to support the prominence and the material falls to the photosphere.

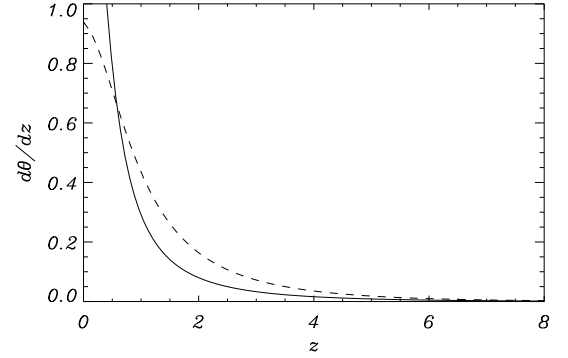


FIG. 14.— Derivative of the shear angle (defined as  $\theta = \arctan(B_y/B_x)$ ) respect to  $z$  at the center of the system ( $x = y = 0$ ) as a function of height. The continuous line corresponds to the case  $l/k = 0.95$  while the dashed line represents the case  $l/k = 0.65$ .

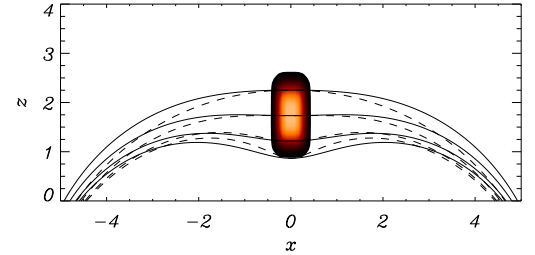


FIG. 15.— Selected magnetic field lines for the case  $l/k = 0.95$  (continuous lines) and  $l/k = 0.65$  (dashed lines). Note the difference in the depth and width of the magnetic dips for the two configurations.

depth of the dips increases with respect to  $l/k = 95$  and thus helping to sustain the mass. On the contrary, the width of the dips is smaller than for the case  $l/k = 0.95$ . Therefore, the magnetic support can be slightly different for the two configurations.

Although in Fig. 12 (bottom panel) the prominence body seems to keep a compact structure, a view from

the top of the configuration (not shown here), reveals a rather different behavior. The dense material tends to move along the magnetic field, and strong deformations appear at the edges of the prominence. In fact, this part of the prominence eventually descends toward the photosphere. This is in agreement with the results of Karpen et al. (2001); Luna et al. (2012) that have found that in a highly sheared arcade with shallow dips the condensation of cool material is short-lived and falls rapidly to the chromosphere. Another effect that we find in the simulations is that in the meantime the orientation of the main axis of the prominence changes with time and tends to be aligned with the direction of the magnetic field. These features, that might be relevant regarding observations, need further investigation but are left for future studies since a detailed analysis would require much longer total simulation times with better spatial resolutions.

It must be pointed out that in the analysis of the dependence of the instability with shear ( $l/k$ ) we have imposed that  $B_2 = B_1$  in Eqs. (6)-(8). This condition selects a particular family of magnetic arcade solutions. Other choices of the constants  $B_1$  and  $B_2$  might lead to the presence of significant dips even for cases where shear is strong. Hence, it might be possible to find configurations with strong shear in which the mass of the prominence does not fall to the photosphere.

#### 4.5. An irregular prominence

Finally, it is important to remark that all the simulations presented in the previous sections are based on the assumption that the initial mass deposition is symmetric. The results are thus affected by this assumption, and among other things, only symmetric modes are excited in the system. Since observations show that in general the distribution of mass in the prominence body is very inhomogeneous it is also interesting to investigate a more general case, and see the effect of inhomogeneity on the numerical experiments. For this reason, here we present the results of a run with an irregular mass. The initial density distribution together with the time evolution are represented in Fig. 16. Most of the initial mass is concentrated around the left part of the prominence, and the interface between the core and corona is not purely horizontal. Again the prominence body is pushing the magnetic field in the negative vertical direction due to the effect of the gravity force. At later times, around  $t = 30$  min, we identify the initial stages of the development of the MRT instability at the curved interface at the bottom of the prominence. Plumes and fingers are again quite evident at  $t = 59$  min. The development of the instability proceeds at a faster rate than in the purely symmetric prominence. Interestingly, these fingers may eventually connect to the photosphere, meaning that the morphology of the structure might evolve from a detached prominence to a hedgerow prominence.

In this simulation since the system is asymmetric the excitation of other types of motions with respect to the symmetric case are possible. For example, in Fig. 17 the velocity component in the  $x$ -direction together with the density are represented as a function of time. Now the point of view has been changed in the plot to better visualize the results. In this plot we identify motions in  $v_x$  that alternate sign with respect to the location of

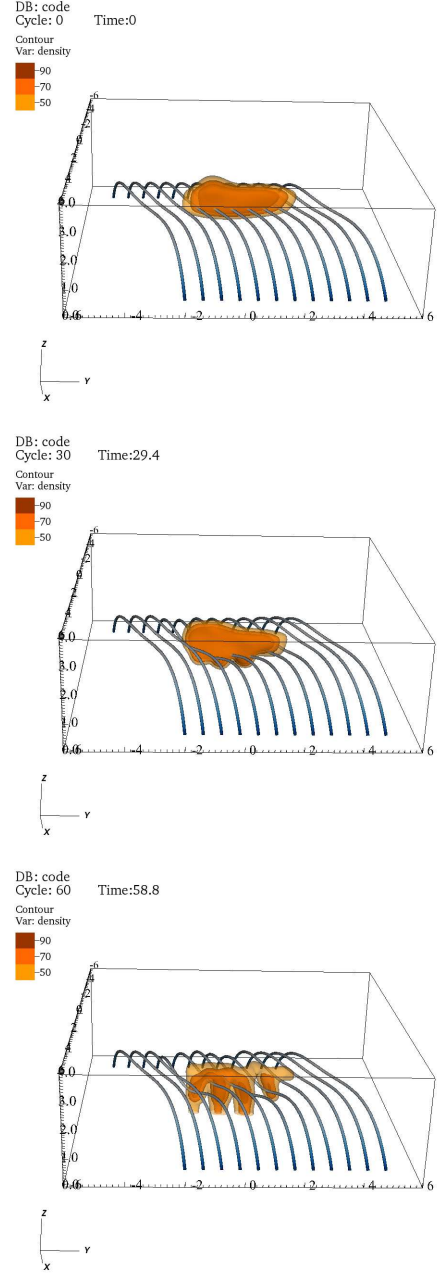


FIG. 16.— Density isocontours at different times. Fingers and plumes associated to the MRT instability are present in this simulation. The difference with respect to Fig. 1 is in the initial shape of the density distribution which is now non-symmetric, the rest of parameters are the same.

the prominence body around the center of the system. These motions are associated to the excitation of perturbations running mostly parallel to the magnetic field and therefore linked to the excitation of slow magnetoacoustic waves (see Terradas et al. 2013, for the equivalent results in 2D). As a consequence of these motions the whole prominence shows changes in the cross-section, as can be appreciated in Fig. 17 (see density isocontours), and at the same time it is oscillating laterally, mostly along the  $x$ -direction (see Movie4). This can have close links with large amplitude longitudinal oscillations reported in the literature (see Tripathi et al. 2009; Zhang et al. 2012;



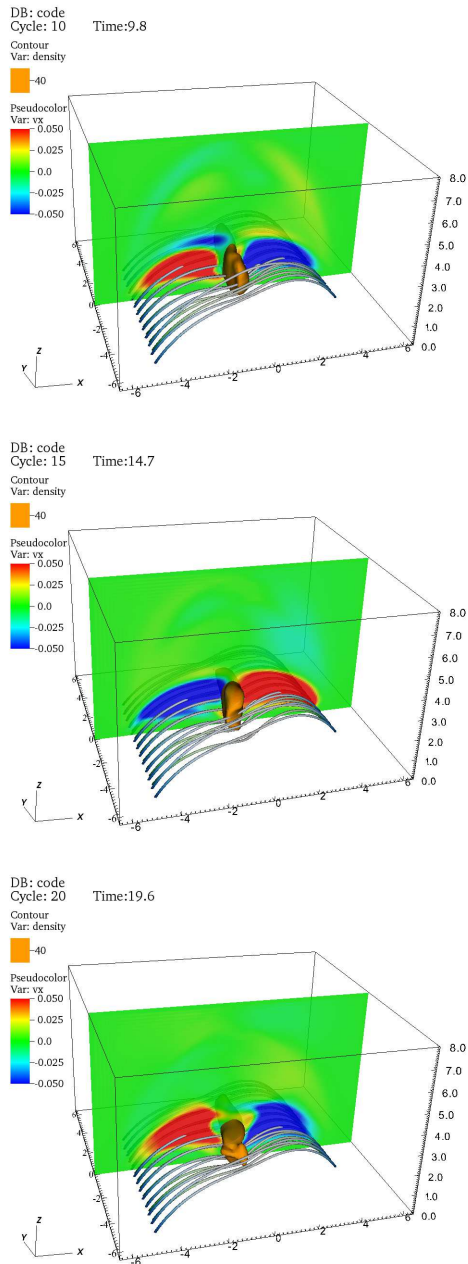


FIG. 17.— Time evolution of density and horizontal velocity at the  $xz$ -plane at  $y = 0$  at the initial stages of the evolution and before the onset of the MRT instability. See Movie4 in the online material.

Luna et al. 2014).

## 5. DISCUSSION AND CONCLUSIONS

We have investigated the time evolution of a simple three-dimensional density enhancement representing a prominence embedded in a sheared coronal arcade. We have studied the evolution of the prominence mass and the magnetic field in a selfconsistent way. This is different respect to other studies about the topology of the magnetic field inferred from photospheric extrapolations since the prominence mass is not taken into account in the model. The results from our study indicate that in general the dynamics of the coupled prominence mass

to the magnetic field is quite involved. We have tried to understand how the results depend on the different parameters of the configuration. A critical parameter that determines the characteristics of the evolution is the plasma- $\beta$ . For low- $\beta$  configurations cold material can be suspended above the photosphere, and it can represent a detached prominences typically reported in observations. In this case there is a balance between the prominence weight, that depends on the mass, and the Lorentz force that changes with the plasma- $\beta$ . A rather different configuration is found when  $\beta$  is increased. In this last case we find that the dense material is essentially moving toward the photosphere and compressing the magnetic field. The overall shape of the structure is more similar to hedgerow or even curtain prominences. Hence, the global morphology of the prominence is highly determined by the plasma- $\beta$  but it is also affected by the boundary conditions at the photosphere. Here, we have focused on line-tying conditions and have found that they are crucial for magnetic support since they communicate the effect of the dense photosphere on the prominence body. The total mass loading of the prominence is also another parameter that determines the morphology and evolution of the structure.

For prominences supported against gravity in the low- $\beta$  regime, we have found fingerprints of the excitation of MRT unstable modes. Fingers and plumes develop on a global scale affecting the whole prominence body. Although the nature of the flows found in our numerical experiments are due to the release of gravitational potential energy, the flow pattern is more complex than in the standard MRT instability at an interface that it is in equilibrium. The reason is that during the development of the instability the prominence is oscillating as a consequence of line-tying conditions and this affects the growth-rates of the modes. The spatial scale of plumes and fingers found in the simulations are much larger than those commonly reported in observations by, for example, Berger et al. (2010) and studied from the numerical point of view by Hillier et al. (2011, 2012a). In our simulations we are simply not resolving those spatial scales due to a lack of spatial resolution. The voids in density found in our simulations can be associated to the appearance of large scale cavities/arches or even bubbles commonly reported in observations, specially in polar crown prominences. Other interpretations have been proposed to explain bubbles, for example Ryutova et al. (2010) have suggested that they are the consequence of the excitation of the kink unstable mode in a flux-rope prominence configuration. Dudík et al. (2012) have proposed that the formation of cavities is due to the emergence of magnetic flux due to the appearance of parasitic bipoles at the photosphere. In any case, it is important to mention that at the prominence body we find vertical structures, linked to the appearance of fingers and plumes, in an essentially horizontal magnetic field. On the contrary, from the observational point of view it is thought that the magnetic field is quite vertical, at least in many curtain and hedgerow prominences formed by vertical threads.

We have showed that magnetic shear stabilizes the configuration. Performing a quantitative study of the dependence of the instability on this parameter we have shown that it can significantly reduce the growth-rates of the



MRT unstable modes. Thus, it has important consequences regarding the stability of the magnetic configuration. In particular, the parameter  $l/k$  in this study is directly related to strength of the magnetic field at the prominence core and to the change of the direction of the horizontal field with height. Strongly sheared configurations have also a fast change of the shear angle with  $z$ , which helps to stabilize the structure (see Ruderman et al. 2014).

In our numerical experiments the transition between the corona and the photosphere has been ignored and line-tying conditions have been applied at  $z = 0$ . A proper analysis of the evolution of prominences attached to the photosphere, like the ones described above (and even suspended prominences), should include the transition region and chromospheric layers. The physics required to reproduce chromospheric or prominence conditions is quite complex (partial ionization effects, radiative transport, etc.). Moreover, thermal effects such as conduction or radiation have been ignored in the present work but are thought to play a relevant role on the shape of the PCTR.

It is clear that the three-dimensional configuration studied here shows very dynamic features and the relaxation to a purely stationary magnetohydrostatic configuration is hardly achieved, at least in the regime of parameters considered in this work. This is different to the two-dimensional case studied by Terradas et al. (2013) using essentially the same magnetic configuration. In that case there were no MRT instabilities because the system was assumed to be invariant with respect to the longitudinal direction (the  $y$ -coordinate in our system) and modes with a component along this direction are in general the most unstable. This indicates, once more, that interpretations based on 2D models may miss important physics. The lack of simple magnetohydrostatic equilibrium also agrees with the observational fact that prominences are locally very dynamic.

Note that although we have not tried to model the prominence formation process (see Xia et al. 2011, 2012; Keppens & Xia 2014, for recent advances about condensations mechanisms with magnetic fields) and the continuous supply of material is missing, we already find

a very complex dynamics. If the formation process is investigated using levitation, injection or condensations models, it will most likely produce even more complex phenomena. This will make things difficult to interpret. For this reason, we have preferred to analyze first the evolution of an existing density enhancement in a coronal environment.

It is worth to mention that it would be interesting to study a flux rope configuration to compare with the present shear arcade model and the embedded direct polarity prominence in order to assess whether there are significant differences in the results. In particular, it would be interesting to understand the role of magnetic twist on the development of the MRT modes as well as on the kink instability. Also, it might be interesting to perform a detailed analysis of the modes of oscillation and to compare with observations of oscillating prominences/filaments induced, for example, by nearby flares. Finally, future studies should use high resolution 3D simulations to resolve the fine structure associated to prominence threads as well as turbulent phenomena related to nonlinearity for a better comparison with observations.

J.T. acknowledges support from the Spanish Ministerio de Educación y Ciencia through a Ramón y Cajal grant. R.S. acknowledges support from MINECO through a Juan de la Cierva grant (JCI-2012-13594), from MECO through project CEF11-0012, and from the Vicerectorat d'Investigació i Postgrau of the UIB. J.T., R.S., R.O. and J.L.B. acknowledge the funding provided under the project AYA2011-22846 by the Spanish MICINN and FEDER Funds. The financial support from CAIB through the “Grups Competitius” scheme and FEDER Funds is also acknowledged. M.L. gratefully acknowledges partial financial support by the Spanish Ministry of Economy through projects AYA2011-24808 and CSD2007-00050. This work contributes to the deliverables identified in FP7 European Research Council grant agreement 277829, “Magnetic Connectivity through the Solar Partially Ionized Atmosphere” (PI: E. Khomenko). We thank the anonymous referee for his/her comments that helped to improve the manuscript.

## REFERENCES

- Antiochos, S. K., Dahlburg, R. B., & Klimchuk, J. A. 1994, *ApJ*, 420, L41
- Arregui, I., Oliver, R., & Ballester, J. L. 2012, *Living Reviews in Solar Physics*, 9, 2
- Aulanier, G., DeVore, C. R., & Antiochos, S. K. 2002, *ApJ*, 567, L97
- Balsara, D. S., Rumpf, T., Dumbser, M., & Munz, C.-D. 2009, *Journal of Computational Physics*, 228, 2480
- Berger, T. E., et al. 2008, *ApJ*, 676, L89
- . 2010, *ApJ*, 716, 1288
- Bona, C., Bona-Casas, C., & Terradas, J. 2009, *Journal of Computational Physics*, 228, 2266
- DeVore, C. R., Antiochos, S. K., & Aulanier, G. 2005, *ApJ*, 629, 1122
- Díaz, A. J., Soler, R., & Ballester, J. L. 2012, *ApJ*, 754, 41
- Dudík, J., Aulanier, G., Schmieder, B., Zapiór, M., & Heinzel, P. 2012, *ApJ*, 761, 9
- Hillier, A., Berger, T., Isobe, H., & Shibata, K. 2012a, *ApJ*, 746, 120
- Hillier, A., Isobe, H., Shibata, K., & Berger, T. 2011, *ApJ*, 736, L1
- . 2012b, *ApJ*, 756, 110
- Hillier, A., & van Ballegoijen, A. 2013, *ApJ*, 766, 126
- Hood, A. W., & Anzer, U. 1990, *Sol. Phys.*, 126, 117
- Jiang, G.-S., & Wu, C.-c. 1999, *Journal of Computational Physics*, 150, 561
- Jones, F. S. 1958, *JRASC*, 52, 149
- Karpen, J. T., Antiochos, S. K., Hohensee, M., Klimchuk, J. A., & MacNeice, P. J. 2001, *ApJ*, 553, L85
- Karpen, J. T., Tanner, S. E. M., Antiochos, S. K., & DeVore, C. R. 2005, *ApJ*, 635, 1319
- Keppens, R., & Xia, C. 2014, *ArXiv e-prints*
- Khomenko, E., Díaz, A., de Vicente, A., Collados, M., & Luna, M. 2014, *A&A*, 565, A45
- Kippenhahn, R., & Schlüter, A. 1957, *ZAp*, 43, 36
- Labrosse, N., Heinzel, P., Vial, J.-C., Kucera, T., Parenti, S., Gunár, S., Schmieder, B., & Kilper, G. 2010, *Space Sci. Rev.*, 151, 243
- Li, T., & Zhang, J. 2012, *ApJ*, 760, L10
- Low, B. C. 1981, *ApJ*, 246, 538
- Low, B. C., & Zhang, M. 2004, *ApJ*, 609, 1098
- Luna, M., Karpen, J. T., & DeVore, C. R. 2012, *ApJ*, 746, 30
- Luna, M., Knizhnik, K., Muglach, K., Karpen, J., Gilbert, H., Kucera, T. A., & Uritsky, V. 2014, *ApJ*, 785, 79

- Mackay, D. H., Karpen, J. T., Ballester, J. L., Schmieder, B., & Aulanier, G. 2010, *Space Sci. Rev.*, 151, 333
- Menzel, D. H., & Evans, J. W. 1953, in *Accademia Nazionale dei Lincei*, Vol. 2, *Covvegno Di Scienze Fisiche Matematiche e Naturali*, ed. R. Mc Math & M. P. Savedoff, 119
- Mikaelian, K. O. 1986, *Phys. Rev. A*, 33, 1216
- Oliver, R. 1999, in *ESA Special Publication*, Vol. 448, *Magnetic Fields and Solar Processes*, ed. A. Wilson & et al., 425
- Oliver, R., & Ballester, J. L. 2002, *Sol. Phys.*, 206, 45
- Powell, K. G., Roe, P. L., Linde, T. J., Gombosi, T. I., & de Zeeuw, D. L. 1999, *Journal of Computational Physics*, 154, 284
- Rayleigh, L. 1883, *Proceedings of the London Mathematical Society*, 14, 170
- Ruderman, M. S., Terradas, J., & Ballester, J. L. 2014, *ApJ*, 785, 110
- Rust, D. M., & Kumar, A. 1994, *Sol. Phys.*, 155, 69
- . 1996, *ApJ*, 464, L199
- Ryutova, M., Berger, T., Frank, Z., Tarbell, T., & Title, A. 2010, *Sol. Phys.*, 267, 75
- Sakurai, T. 1976, *PASJ*, 28, 177
- Schutgens, N. A. J. 1997, *A&A*, 323, 969
- Shen, Y., Ichimoto, K., Ishii, T. T., Tian, Z., Zhao, R., & Shibata, K. 2014, *ApJ*, 786, 151
- Shu, C.-W. 2009, *SIAM Review*, 51, 82
- Taylor, G. 1950, *Royal Society of London Proceedings Series A*, 201, 192
- Terradas, J., Andries, J., Goossens, M., Arregui, I., Oliver, R., & Ballester, J. L. 2008, *ApJ*, 687, L115
- Terradas, J., Soler, R., Díaz, A. J., Oliver, R., & Ballester, J. L. 2013, *ApJ*, 778, 49
- Török, T., & Kliem, B. 2003, *A&A*, 406, 1043
- Török, T., Kliem, B., & Titov, V. S. 2004, *A&A*, 413, L27
- Tripathi, D., Isobe, H., & Jain, R. 2009, *Space Sci. Rev.*, 149, 283
- Tsubaki, T. 1988, in *Solar and Stellar Coronal Structure and Dynamics*, ed. R. C. Altrock, 140–149
- van den Oord, G. H. J., Schutgens, N. A. J., & Kuperus, M. 1998, *A&A*, 339, 225
- Xia, C., Chen, P. F., & Keppens, R. 2012, *ApJ*, 748, L26
- Xia, C., Chen, P. F., Keppens, R., & van Marle, A. J. 2011, *ApJ*, 737, 27
- Yang, B. L., Wang, L. F., Ye, W. H., & Xue, C. 2011, *Physics of Plasmas*, 18, 072111
- Zhang, Q. M., Chen, P. F., Xia, C., & Keppens, R. 2012, *A&A*, 542, A52
- Zirin, H. 1998, *The Astrophysics of the Sun*